Preprint Title	Crystalline and Amorphous Structure Selectivity of Ignoble High-Entropy Alloy Nanoparticles during Laser Ablation in Organic Liquids is Set by Pulse Duration
Authors	Robert Stuckert, Felix Pohl, Oleg Prymak, Ulrich Schürmann, Christoph Rehbock, Lorenz Kienle and Stephan Barcikowski
Publication Date	10 Feb 2025
Article Type	Full Research Paper
Supporting Information File 1	SI_BJNANO_Stuckert.docx; 5.9 MB
Supporting Information File 2	SI_Insitu_heating_SAED_komp2.mp4; 14.7 MB
ORCID® iDs	Robert Stuckert - https://orcid.org/0009-0009-1273-3205; Stephan Barcikowski - https://orcid.org/0000-0002-9739-7272

Crystalline and Amorphous Structure Selectivity of Ignoble High-Entropy Alloy Nanoparticles during Laser Ablation in Organic Liquids is Set by Pulse Duration

Robert Stuckert[1], Felix Pohl[2], Oleg Prymak[3], Ulrich Schürmann[2,4], Christoph Rehbock[1], Lorenz Kienle[2,4], and Stephan Barcikowski[*1]

Address: [1]Technical Chemistry I and Center for Nanointegration Duisburg-Essen (CENIDE), University of Duisburg-Essen, Universitaetsstr. 7, 45141 Essen, Germany, [2]Institute for Material Science, Synthesis and Real Structure, Faculty of Engineering, Christian-Albrechts University of Kiel, Kaiserstraße 2, 24143 Kiel, Germany, [3]Inorganic Chemistry and Center for Nanointegration Duisburg-Essen (CENIDE), University of Duisburg-Essen, Universitaetsstr. 7, 45141 Essen, Germany, and [4]Kiel Nano, Surface and Interface Science (KiNSIS), Carl-Albrechts University of Kiel, Christian-Albrechts-Platz 4, 24118 Kiel, Germany.

Email: Stephan Barcikowski – Stephan.barcikowski@uni-due.de

* Corresponding author

Abstract

High-entropy alloy nanoparticles (HEA NPs) represent a promising material class with significant potential in various applications like heterogeneous catalysis or magnetic

devices, due to their exceptional compositional tunability arising from the synergistic interplay of multiple elements within a single particle. While laser-synthesized, ligand-free colloidal HEA NPs have already been reported, the underlying formation mechanism remains unknown, particularly the underexplored preference of amorphous metallic glass over crystalline structures warrants further investigation. Herein, we present a systematic study of laser-generated equimolar CrMnFeCoNi nanoparticles, focusing on structural differences, arising from varying pulse durations during synthesis in organic solvents (acetone, ethanol, acetonitrile). In a systematic experimental series using high-resolution transmission electron microscopy (HRTEM), scanning transmission electron microscopy with energy-dispersive X-ray spectroscopy (STEM-EDS), selected-area electron diffraction (SAED), X-ray diffraction (XRD), *in situ* heating, post-irradiation experiments, and differential scanning calorimetry (DSC) we demonstrate that the internal phase structure of the produced NPs is primarily driven by the laser pulse duration and is independent of the used solvent. While picosecond-pulsed laser ablation in liquid (ps-LAL) produces polycrystalline HEA NPs, nanosecond-pulsed laser ablation (ns-LAL) favors a metastable amorphous structure. Particle cores in all cases exhibit a homogeneous distribution of the metals Cr, Mn, Fe, Co, and Ni, while particle shells were found to vary between manganese-enriched oxide layers and thin graphitic carbon coatings. The discovery of the structure-directing mechanism allows one to select between crystalline or amorphous HEA NP products, simply by choice of the laser pulse duration in the same, well-scalable setup, giving access to colloidal particles that can be further downstream processed to heterogeneous catalysts or magnets. In that context, the outstanding temperature stability up to 375°C (DSC) or 500°C (TEM) may motivate future application-relevant work.

Keywords

laser processing in liquids, compositionally complex alloy, complex solid solution, multicomponent alloy, cantor alloy, metallic glass, TEM-EDS, selected area electron diffraction, X-ray diffraction

Introduction

High-entropy alloys (HEAs), also referred to as compositionally complex solid solutions (CCSS) [1], are of great interest in various applications as in magnetic technologies [2, 3] and electrocatalysis [2, 4], deriving from the combination of single-element properties that result in enhanced features, compared to single-element properties [5]. High-entropy alloy nanoparticles (HEA NPs) constitute a relatively new class of nanomaterials, usually consisting of single-phase solid solutions made of five or more elements, forming relatively simple face-centered cubic [6–8] (fcc) or body-centered cubic [9, 10] (bcc) crystal structures, stabilized by the entropic part of Gibbs-free energy. It is worth noting that high-entropy stabilization is highly disputed and the often discussed core effects of HEA do not apply to every element system [11, 12]. Still we decided to refer to the term HEA in this work as it is deeply rooted within the community, despite the existence of names like CCSS, complex concentrated alloys, compositionally complex alloy, deriving from the critical view of the high-entropy effect [1]. The symbiosis of multiple elements leading to potential highly effective properties was already shown in energy applications [13] and particularly in the field of heterogeneous catalysis, boosting efficiencies in ammonia decomposition [4], oxygen evolution reactions (OER) [14], oxygen reduction reactions (ORR) [15], in CO oxidation [16], and in CO_2 and CO reduction [17]. This high activity in catalysis has been

attributed to adsorption energy distribution patterns (AEDP) during catalytic reactions [18], that may be tuned based on DFT calculations of binding energies and machine learning algorithms for an efficient catalyst design [15, 17, 19]. The synthesis of HEA NPs has been realized by many methods like carbothermal shock synthesis (CTS) [20, 21], chemical reduction [22, 23], fast-moving bed pyrolysis [24], solvothermal methods [25], and more, as addressed in several review articles [26–29]. In brief, the usual structures yielded when synthesizing HEA NPs are mostly fcc and bcc. Applying CTS, Yao et al. reported quinary, senary, septenary, and even octonary HEA NPs, all forming a fcc lattice [20] and the synthesis of the CrMnFeCoNi system by arc-discharge plasma method also lead to the formation of fcc HEA NPs [7]. The addition of Al to the high-entropy alloy system was shown to stabilize a bcc-type structure in the synthesized HEA NPs [14, 30] while amorphous $FeCoNiCrMo_x$ HEA NPs could also be synthesized by inert gas condensation as stated very recently by Zhou et al. [31]. However, none of these above-mentioned synthesis techniques give access to colloidal HEA NPs but to structures bound to an often very specific support material or limited to gas phase conditions. An approach for the synthesis of colloidal HEA NPs is magnetron sputtering, though special requirements like vacuum stable solvents, e.g., ionic liquids limit its widespread use [32], and scalability is limited. Colloidal NP products have several advantages, e.g., in the fabrication of heterogeneous catalysts colloids are more flexible as the support material is not predefined by the synthesis route but can be chosen freely. Additionally, in contrast to form-in-place-methods like CTS [20], the NP size does not depend on the loading [33].

Nanoparticle generation by laser synthesis and processing of colloids (LSPC) [34–37] provides nanoparticles dispersed in liquids without the addition of organic additives or support material to stabilize the particles with high variability on the used solvent,

yielding colloidal nanoparticles with productivities up to 8 g/h [38]. The throughput linearly scales with the laser power [39], so that energy-specific mass productivity values are useful scaling factors. Here, the experimentally determined values of 9.7 µg/J [38] align with those from computational works (5 – 7 µg/J) [40]. Depending on the set goal, colloidal nanoparticles can be synthesized and/or processed by laser ablation in liquid (LAL) [41–45], laser fragmentation in liquid (LFL) [46, 47], and laser reduction in liquid (LRL) [48–50], making LSPC an efficient method for nanoparticle research but also for scale-up. Furthermore, procedures for LAL are usually not bound to strict limitations when it comes to pressure and solvent, as for example in magnetron sputtering techniques. Colloidal HEA NPs by LSPC were first reported in 2019 by Waag et al. [51], where CrMnFeCoNi NPs were produced in ethanol, using a ps-pulsed laser for ablation (ps-LAL), yielding colloids of HEA NPs with a mean diameter below 10 nm and productivities of 3 g/h. Both the bulk target and the NPs showed a crystalline fcc phase with a lattice parameter of 3.58 Å and a solid solution structure. Löffler et al. investigated the very same element system enriched with Mn, again made by ps-LAL in ethanol, also reporting particle mean diameters below 10 nm and solid solution fcc structure, whereas this study was more focused on the applicability in catalysis [18]. By irradiating metal chloride salts, premixed in ethanol and then added to a hexane solution with oleic acid present, Wang et al. successfully synthesized PtIrCuNiCr NPs with a narrow size distribution and uniformly mixed elements within the generated nanoparticles [52]. Recently, Tahir et al. conducted ps-LAL on the CrMnFeCoNi system in ethanol and varied production methods for the bulk targets, showing uniformly mixed HEA NPs with a fcc structure and indications for a minor fraction of oxidized manganese [53]. Johny et al. used ns-pulsed LAL in acetonitrile to fabricate colloidal CrMnFeCoNi and CrMnFeCoNiMo HEA NPs with an amorphous metallic

glass crystal structure and only minor contributions from crystalline phases [54]. As LSPC methods are based on ultrashort (fs, ps) or short (ns) pulsed lasers, unparalleled high cooling rates occur [55, 56], resulting in distinct NP undercooling [40], creating defects-rich NP structures [33, 57, 58]. Despite these high cooling rates, LSPC-fabricated metal or alloy NPs are usually crystalline. At the example of immiscible binary alloys, it has been clarified that LAL can be classified as a kinetically controlled synthesis method, with nanothermodynamic contributions that set the final NP structure during cooling [59]. Hence, thermodynamically metastable NP structures are generated that are stable at elevated temperatures [60] and even under harsh thermocatalytic [57] and electrocatalytic [58] reaction conditions.

Even though amorphous metallic glass NPs are generally well-studied [61–65], their synthesis by LSPC is still in its infancy as recently highlighted [66], though a few basic rules could be derived from previous LSPC synthesis studies [67, 68], namely very high cooling rates, the presence of at least three constituting elements, atomic size differences over 12 %, a significant negative heat of mixing of major elements, small material dimensions (preferably on the nano-scale, favoring high cooling rates), and post-processing effects. Furthermore, metalloid elements such as phosphorous, silicon, boron, and carbon were shown to retard crystallization and favor the formation of long-range disordered structures. Organic solvent molecules used in LSPC can serve as a carbon source which strongly affects the stabilization of amorphous structures while the influence of the other mentioned metalloids is less frequently observed [66]. Crystalline FeSiB NPs, synthesized by ns-LAL in water could be modified and an amorphous structure could be achieved by a follow-up LFL treatment. As a result, the particle size decreased and the beforehand dominant α-Fe structure could not be observed after LFL, and solely amorphous structures were found [67]. Ps-

LAL on FeSiB in organic solvents, however, yielded amorphous NPs directly after ablation in acetone, ethanol, and acetonitrile, while nanocrystalline byproducts of α-Fe/Fe_3C phases were also detected after synthesis in ethanol [68]. Recently, Su et al. showed amorphization of wet-chemically synthesized crystalline FeNi NPs encapsulated in N-doped carbon nanotubes by re-irradiating the samples with a pulsed laser beam [69]. In brief, amorphous alloy NPs by laser-based synthesis techniques are not well studied though representing an emerging field due to applicability in catalysis. In particular, amorphization of HEA NPs from LSPC has only been reported in one study [54] and it is unknown which factors determine if the produced particles are crystalline or amorphous.

Herein, we report on the laser synthesis of colloidal Cantor alloy (CrMnFeCoNi) NPs systematically varying both pulse duration (ps-LAL and ns-LAL) and organic solvent (acetone, ethanol, acetonitrile) aiming to deduce general design rules triggering the formation of crystalline or amorphous structures in the corresponding particles. Nanoparticle characterization is done by HRTEM, STEM-EDS, SAED, and XRD, complemented by tempering and laser post-irradiation experiments to pinpoint HEA NP formation pathways under thermodynamic or kinetic control.

Results and Discussion

Ps- and ns-LAL of the bulk target in all solvents yielded colloids at mass concentrations of 100-200 mg/L, determined by differential weighing of the target before and after ablation. The total compositions of the colloids in acetone were determined by STEM-EDS and were similar for both laser pulse durations, namely $Cr_{22}Mn_{16}Fe_{21}Co_{20}Ni_{20}$ for colloids made by ps-LAL and $Cr_{21}Mn_{21}Fe_{20}Co_{19}Ni_{19}$ for colloids fabricated by ns-LAL (global values determined via STEM-EDS displayed in

Table S1 and Table S2). These values are in good agreement with the near-equimolar composition of the bulk target ($Cr_{21}Mn_{18}Fe_{21}Co_{18}Ni_{22}$), determined by both XRF and SEM-EDS measurements, quantifying not only the surface compositions of the corresponding targets but also bulk compositions determined from a target cross-section (Figure S2).

Pulse duration effects on the crystal structure and composition

The first objective of this study was to investigate the influence of pulse durations during LAL in organic solvents (all dried, distilled, and degassed) on the crystal structure and composition of the corresponding HEA NPs. Figure 1 shows a representative result of colloids from LAL in acetone analyzed by SAED on ensembles of 300-400 HEA NPs. These findings highlight the formation of crystalline particles with fcc structure and estimated d-values of 2.09 Å (111), 1.83 Å (200), and 1.29 Å (220) during ps-LAL (Figure 1A). This is in good agreement with former ps-LAL studies by Waag et al. and also by Löffler et al., who both reported comparable d-values of 2.08 Å (111), 1.81 Å (200), and 1.28 Å (220), determined by both SAED and XRD analysis [18, 51]. Contrary, amorphous structures are found during ns-LAL (Figure 1D), showing no Bragg reflections. This observation was also confirmed by HRTEM micrographs of representative particles where a (111)-lattice spacing with a d-value of 2,08 Å (Figure 1C) is observable for NPs from ps-LAL, being in good agreement with the estimated value in the bulk target (d(111)-value of 2,08 Å, compare Figure S2). In contrast, Figure 1F shows the HRTEM micrographs of an amorphous particle, resulting from ns-LAL in acetone. As the number of analyzed particles is similar in the SAED-analysis data from Figures 1A and D, a dependency of the crystal structure in ignoble HEA NPs on pulse duration (ps vs. ns) is hypothesized. To further investigate this hypothesis, we looked at further potential influence factors such as a potential

dependency on particle sizes, solvent type, deviating compositions in the ablated bulk targets and HEA NPs, laser fluence, and post-irradiation effects.

One assumption may be that amorphization is ruled by the particle diameter as it is well-known that smaller NPs may appear amorphous in XRD due to less coherent conditions for Bragg reflection from their crystalline domains [70, 71]. To test this hypothesis, we analyzed the particle size distributions within the circular areas used for SAED experiments for amorphous samples from ns-LAL and crystalline samples from ps-LAL. Figure 1B and E show TEM images of analyzed HEA NPs with the corresponding particle size distributions directly associated with the diffraction patterns of the SAED analysis. In both selected areas (indicated as white circles in Figures 1B and 1E, respectively) the determined particle size distributions show mean values of 21 ± 10 nm for crystalline ps-ablated particles and 21 ± 7 nm for amorphous ns-ablated particles. Based on these findings we can conclude that the pronounced differences in crystallinity in the samples cannot be explained by differences in particle diameters. However, a certain width of the size distribution curves indicated by the polydispersity indices (PDI) (PDI=0.31 for ps-LAL HEA NPs and PDI=0.12 for ns-LAL HEA NPs) is evident. Due to fundamental differences in the particle formation mechanisms during ps- and ns-LAL as proposed by Shih et al., ps-LAL has been reported to yield bimodal size distributions (at least of Ag and Au at high fluences) [72], which may be the reason for the broader size distributions in ps-LAL. Note that Waag et al. reported mean particle sizes of 10 nm during ps-LAL of equimolar CrMnFeCoNi in ethanol [51]. This difference is most likely attributed to the fact that size analysis in their work refers to hydrodynamic diameters obtained from analytical disk centrifugation where a significantly higher quantity of nanoparticles can be analyzed, while in our work TEM was used to directly image individual particles. This difference is clarified by a comparison between the mean particle sizes in the other solvents

ethanol and acetonitrile [54], that have mean diameters comparable to the samples in acetone (Figure S3) when analyzed by TEM images. The similarity in particle sizes of Figure 1B and E with the absence of SAED reflections in ns-LAL HEA NPs indicate that the results are independent of the signal-dominant mean particle size of the sample.

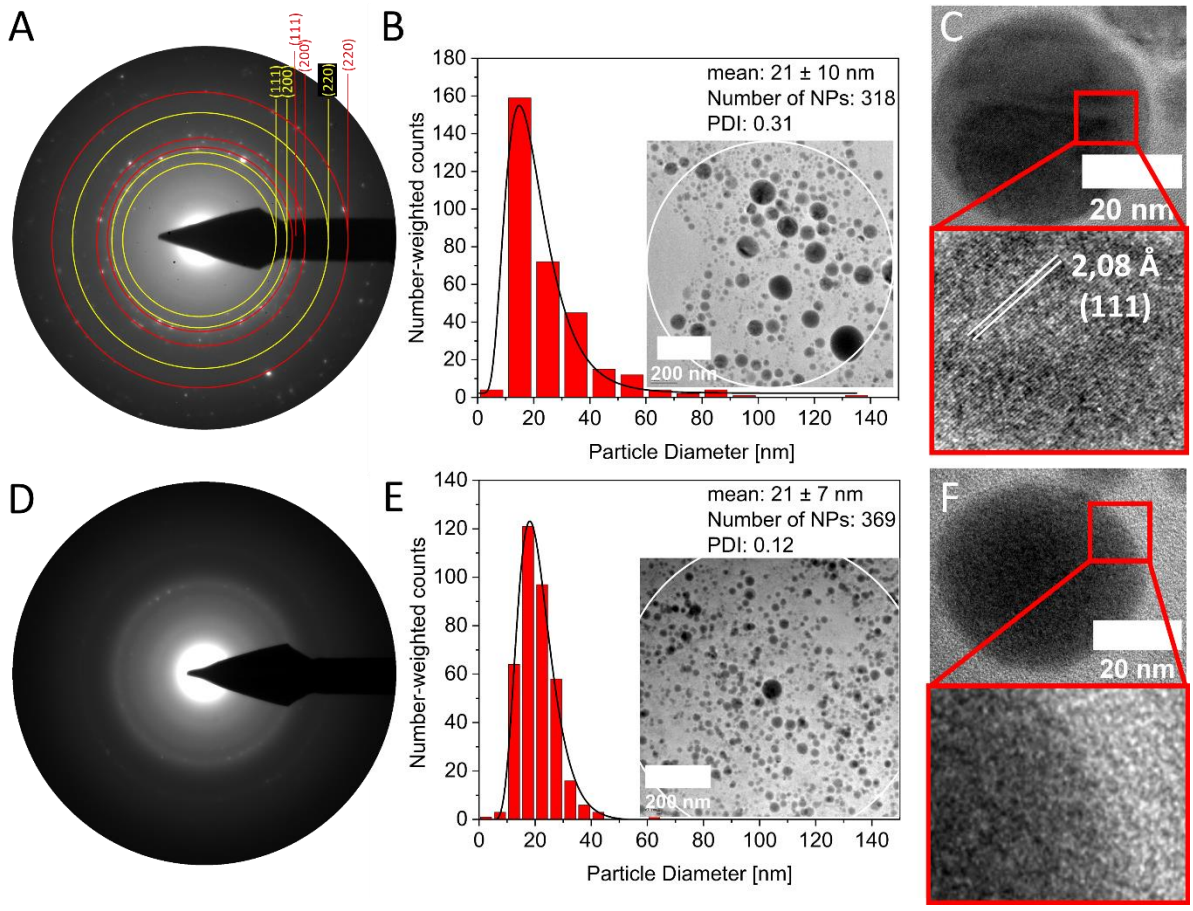

Figure 1: SAED pattern of ps-ablated crystalline HEA NPs (red: reflections assigned to fcc and yellow: reflections assigned to MnO) (A) and the corresponding analyzed area with particle size distribution with a mean diameter of 21 ± 10 nm (B) and ns-ablated amorphous HEA NPs (D), also with its corresponding analyzed area as well as particle size distribution with a mean diameter of 21 ± 7 nm (E). Analyzed areas for SAED and size distribution are marked with white circles in TEM images. (C) depicts an HRTEM micrograph of a crystalline HEA NP, made by ps-LAL, representing an fcc

structure with a $d_{(111)}$-value of 2.08 Å and (F) shows an amorphous particle, by ns-LAL, exhibiting no structural motif.

Solvent type variation

To test whether amorphization tendencies are, furthermore, dependent on the solvent used, we conducted additional ns-LAL in ethanol and ps-LAL in acetonitrile complementary to studies previously reported by Waag et al. [51] (ps-LAL in ethanol for CrMnFeCoNi) and Johny et al. [54] (ns-LAL in acetonitrile also for CrMnFeCoNi). The corresponding data are presented in the supplementary information (Figure S3) and clearly show no dependency of amorphization on the three tested solvents acetone, ethanol, and acetonitrile. In all solvents ns-LAL leads to amorphous NPs while during ps-LAL the particles were crystalline.

Crystallography and (traces of) oxidation

Further investigations on HEA NPs are required to determine whether the structural information obtained from Figure 1 can also be reproduced for a larger fraction of the samples. Thus, XRD measurements were conducted on both ps- and ns-ablated HEA NPs. Figure 2 shows representative diffraction patterns of ps-ablated HEA NPs and ns-ablated HEA NPs (Figure 2A), both synthesized in acetone. The particles from ps-LAL show a distinctive crystalline fcc diffraction pattern of CrMnFeCoNi NPs reflections at the diffraction angles 2θ = 43.3 °, 50.5 °, and 74.1 ° and the corresponding lattice parameter of 3.635 Å as determined by Rietveld refinement, which agrees well with the lattice parameters of the bulk target (3.601 Å) (Figure S2) and those from previous studies [51]. Note that the small difference in the lattice constants between NPs and bulk could be attributed to lattice strain in the particles resulting from rapid heating and cooling processes with rates of up to 10^{13} K/s [40] during LAL. An average crystallite

size of 10 nm was determined, which indicates the presence of polycrystalline HEA NPs. Additionally, a broad (110)-intensity of manganese(II)-oxide can be detected at 35.6 ° with a crystallite size calculated to be 3 nm. Thin oxide shells, mainly formed by manganese oxide species, can be found in STEM and TEM images from ps- and ns-synthesized NPs (compare Figure S4) and could be one explanation for the oxide phase detected in the XRD analysis of Figure 2A. Note that aside from oxide shells, carbon shells were also found in some of the observed HEA NPs in both ns-LAL and ps-LAL (exemplary shown in Figure S4). In general, not all HEA NPs were found to possess oxide or carbon shells resolvable by TEM. Compared to the results from Johny et al. who synthesized HEA NPs in acetonitrile by ns-LAL and observed prominent carbon shells [54], the amount of carbon shells after ps- and ns-LAL in acetone is significantly less, so we can conclude that LAL in acetone yields both oxide and carbon encapsulated HEA NPs while particles without observable shell formation were also found.

In a direct comparison of the X-ray diffraction patterns in Figure 2 (ns vs. ps), the diffraction pattern of ns-LAL HEA NPs shows a significant decrease in crystallinity (Figure 2A, red line). As comparable masses of NPs were analyzed in each XRD analysis, it is not relatable to a lack of X-ray intensity from the sample volume. Even though the diffraction patterns of ns-LAL HEA NPs confirm that mainly amorphous HEA NPs are present, a small amount of crystalline structures contribute to the (111)-reflection of the fcc structure (average crystallite size = 10 nm). This follows a study by Johny et al., where the authors also reported a small amount of larger crystalline particles after ns-LAL of Cantor alloy NPs in the sample by XRD, among the dominant amount of amorphous particles [54]. Additionally, a few sharper reflections from unknown phases, having crystallite sizes between 40 to 50 nm (after anisotropic refinement) could be detected (marked by red arrows in Figure 2B), but due to their

weak intensity, an identification was not possible. The presence of those unidentified reflections is most likely due to the formation of minor mass fractions of HEA NPs exceeding a particle diameter of several hundreds of nanometers, which are partially crystalline. To selectively analyze the larger particle fractions with diameters > 100 nm, single particle SAED analysis was conducted (Figure 2 D-F). Interestingly, structural heterogeneity was observable at this size regime. While the first two particles are still fully amorphous and thus strengthen our hypothesis that amorphization is not linked to particle size, the particle in Figure 3F shows two reflections, although they do not result from a metallic fcc structure. With d-values of 1.09 Å and 0.98 Å, they are most likely attributed to multiple-element oxides such as (FeMn)O. As such species cannot be identified in the diffractogram, we can conclude that those oxides are not formed in the majority of the HEA NPs. Based on these complementary findings from XRD and single particle SAED we can summarize that reflections found in the otherwise amorphous samples are not attributed to a size-dependent difference in crystal structures but are probably derived from minor crystalline oxide phases. To further highlight that amorphization occurs independent of the used solvent, XRD analysis was also conducted on particles synthesized in ethanol (see Figure S5). Here intensity differences between ps-LAL and ns-LAL HEA NPs are even more pronounced. Comparing the observed reflections in single-particle SAED with the unknown reflections in the X-ray diffractogram of Figure 2A and B, we see that the unknown reflections most likely result from oxide phases, although the minor contribution of the (111)-reflection from XRD could not be found in the larger HEA NPs by ns-LAL in single-particle SAED. Thus, we cannot fully exclude the presence of a minor fraction of crystalline particles during ns-LAL although the vast majority is confirmed to be amorphous.

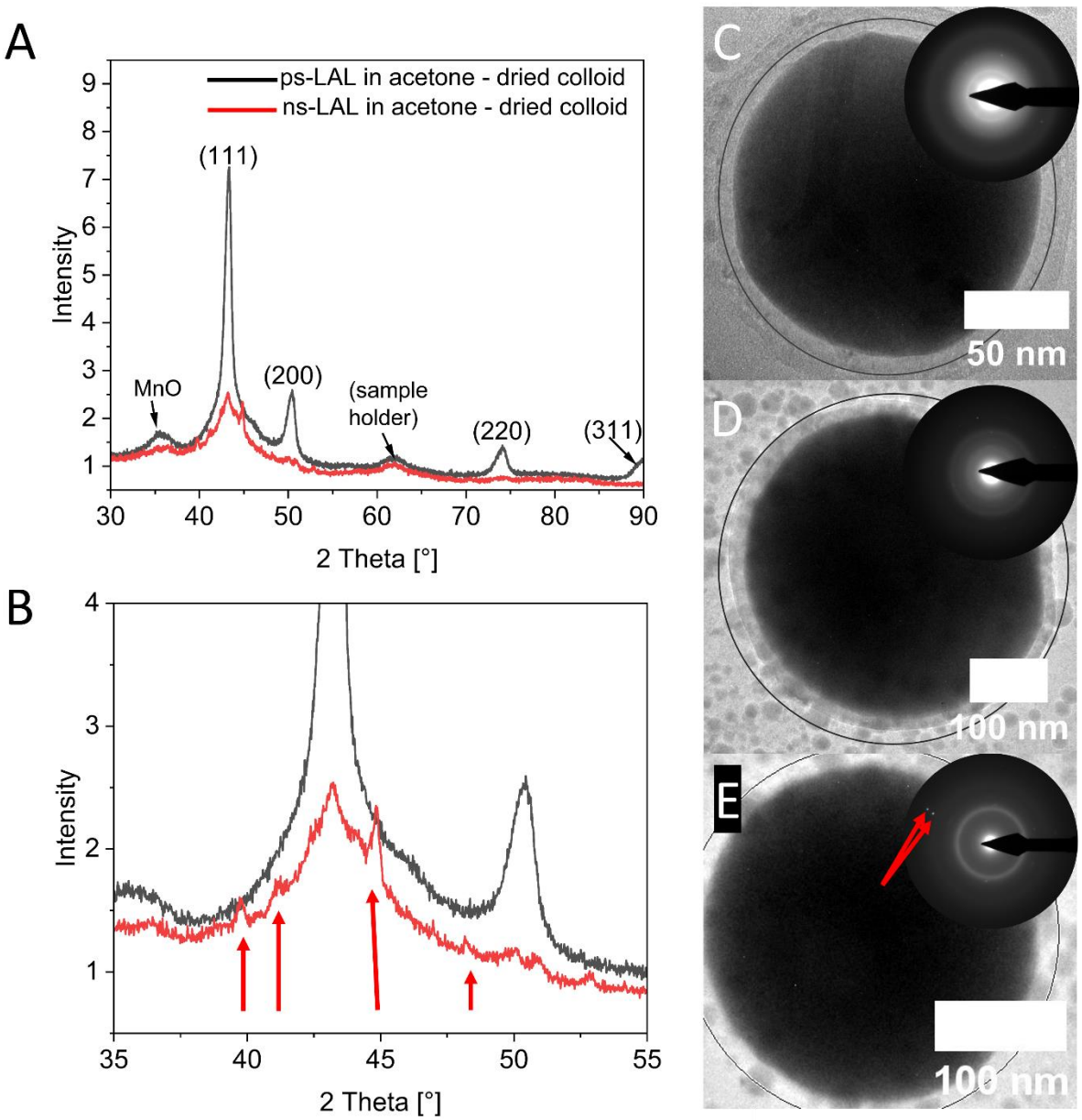

Figure 2: X-ray diffraction patterns of ps-LAL and ns-LAL HEA NPs, indicating a decrease in crystallinity in ns-LAL HEA NPs (A) and a magnified area (B) with arrows depicting unknown phases with relatively sharp reflections of crystallite sizes between 40 – 50 nm in ns-LAL HEA NPs. (C, D, E) Selection of particles by ns-LAL with diameters above 100 nm and the single-particle SAED as an insert, showing that big particles are formed fully amorphous (C, D) or with minor crystalline reflections (indicated by red arrows) (E). Grey circles in C-E indicate the analyzed area for single-particle SAED analysis.

As different pulse durations (ps vs. ns) may lead to fundamentally different ablation mechanisms during LAL [40, 55], it is conceivable that differences in sample compositions (content and distribution of the elements Cr, Mn, Fe, Co, Ni) may be responsible for the observed pulse duration dependent differences in crystal structures. To examine this issue, we initially analyzed the crystal structure of the bulk target via XRD (Figure S2). The structure of the target is characterized by two fcc structures with lattice constants of 3.601 Å and 3.595 Å with average crystallite sizes of 108 nm and 153 nm, respectively. Furthermore, the elemental composition of the target was analyzed by EDS and XRF, differentiating compositions on the upper and lower surface of the target as well as the core composition determined by EDS after target slicing. The overall composition of the elements in the target is fully homogeneous though it should be noted that the diameter of the used SEM-EDS probe beam is 1 µm, so potential differences in the composition between the different crystallites with average diameters of 108 and 153 nm may not have been resolved. So, it is conceivable that small differences in the composition of the crystallites may have been responsible for the occurrence of two fcc phases. The determined values considering crystallite size and lattice constants by XRD agree with former studies on this element system in the bulk state [73]. In consecutive experiments, we also analyzed the elemental composition of the targets after ps-LAL and ns-LAL using EDS. The findings show that the surface retains its homogeneous distribution of elements and no favored ablation of single elements with resulting element islands from non-ablated elements can be observed. Thus, besides some topographic differences visible at high magnifications due to the melting process in ns-LAL, no significant differences can be seen on the bulk targets' surface after each ablation. Based on this data we can conclude that element ratios close to the bulk mole fraction of the target are converted into NPs (Figure S6).

High resolution particle characterization

However, the elemental distribution on a single particle level may still be different between NPs from ns- and ps-LAL. To this end, the formed HEA NPs were examined by STEM-EDS analysis. A homogeneous element distribution confirmed by EDS maps and representative EDS line scans is observed for both crystalline particles by ps-LAL (Figure 3A), as well as amorphous particles by ns-LAL (Figure 3B). The oxygen signals, equally pronounced in NPs from ps- and ns-LAL hint towards oxidation of the particles. Even though these measurements cannot differentiate between an oxidized surface and an oxidized core of the particle, its horizontal progression of oxygen signal hints towards surface oxidation. This follows the XRD results (Figures 2A and B) where reflections attributed to MnO were identified, most likely resulting from thin oxide layers on top of metallic HEA NPs as can be seen in Figure S4. Oxidation of HEA nanoparticles was already reported by Johny et al. and also Tahir et al., including atom probe tomography analysis, showing that oxidation processes in LAL in organic liquids cannot be prevented completely (but at least down to a few at%) [53, 54]. In some cases, a depletion of Mn is seen in exemplary HEA NPs when the composition of single particles is analyzed (see Tables S4 and S5, section S10) which was also observed in the work by Johny et al. [54] and Tahir et al. [53]. This is most likely due to the lowest melting point and highest vapor pressure of Manganese in this element system [74, 75], but also due to its negative redox potential and high oxygen affinity that favors Mn leaching based on chemical mechanisms [19]. Due to the small crystallite size of 3 nm, calculated from the Mn oxide reflections in both ps-HEA NPs and ns-HEA NPs (Figures 3A and 3B) the existence of small MnO precipitates is also possible, which may explain the lack of elemental Mn in individual HEA NPs, while global EDS compositions are comparably close to the bulk target. Generally, the composition of metallic constituents

in all HEA NPs analyzed agrees well with the determined composition of the bulk target which was conducted by both EDS and XRF analysis (Figure S2, Section S2, and Section S10).

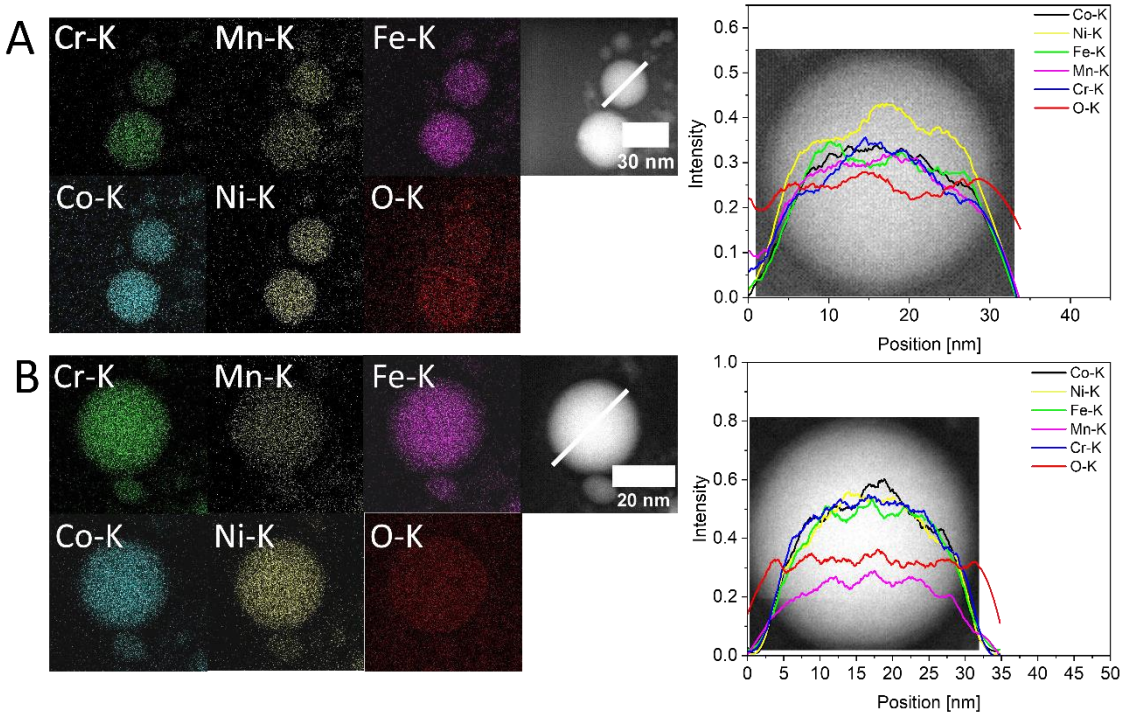

Figure 3: STEM-EDS characterization of HEA NPs by ps-LAL (A) and ns-LAL (B) with EDS maps of Cr, Mn, Fe, Co, Ni, and O, all signals extracted from K-shell and additional line scans of chosen particles. The positions of the line scans are both marked in the STEM images to the corresponding EDS maps. All elements are mixed homogeneously within the particles and show no qualitative differences between the two synthesis methods.

Note that the previous LAL experiments to fabricate HEA NPs in this work were conducted using lasers with strongly deviating pulse energies and laser fluences (0.1 J/cm² for ps-LAL and 7 J/cm² for ns-LAL). To verify that the fluence used in our study does not influence the amorphization, we conducted control experiments at the same laser fluence of 1.6 J/cm² for both pulse durations (corresponding parameters

can be found in Table S3, Section S8) which lies in the high fluence regime, exceeding typical threshold fluences by far [40, 76]. As depicted in Figure S7, amorphization tendencies were analogous to the experiments conducted at the fluences mentioned above. Based on these findings we conclude that deviations in fluence cannot account for the formation of amorphous and crystalline structures in CrMnFeCoNi HEA NPs.

Post-irradiation control experiments

Based on these experimental series we can conclude that the pulse duration during LAL synthesis of CrMnFeCoNi HEA NPs is the main discriminator driving the prevalence of amorphous or crystalline phase structures. But how does the pulse duration affect the particle´s structure? To resolve this conundrum, we first need to clarify whether amorphization is a phenomenon that occurs directly during particle formation or whether post-irradiation effects are involved. As stated in the experimental section, LAL was conducted in a stirred semi-batch ablation chamber described elsewhere [77] whose constructional design is shown in Figure S1. A part of the stirred ablation liquid is constantly in front of the bulk target and is thus constantly irradiated by the pulsed laser beam. Consequently, the number of laser pulses per particle changes with ablation time. A previous study by Su et al. shows amorphization of nanoparticles after laser post-processing [69], indicating a potential interplay between amorphization and post-irradiation. To understand whether the amorphization in ns-LAL HEA NPs is a result of post-irradiation, freshly formed crystalline particles, the crystalline HEA NPs made by ps-LAL, were irradiated with ns-pulses at a wavelength of 1064 nm. Vice versa, we also checked whether amorphous NPs derived from ns-LAL could be crystallized by post-irradiation with ps-pulses. As can be seen in Figure 4A and Figure S8, the results show that post-irradiating HEA NPs does not affect the crystallinity of the particles in both cases. To highlight this, Figure 4A shows the

electron diffraction patterns and number-weighted size distributions of HEA NPs by ps-LAL (left) and the particles after irradiating with ns-pulses (right). Interestingly, the crystallinity of the particles does not change after irradiation and the fcc structure is stable against the irradiation with d-values of 2.09 Å (111), 1.83 Å (200), and 1.29 Å (220) (marked red) and additional reflections mainly resulting from MnO- but also from other potential unknown oxide species (marked yellow). This diffraction pattern is thus comparable with the pattern of the particles before the experiment (Figure 4A left), having the same d-values for the fcc structure.

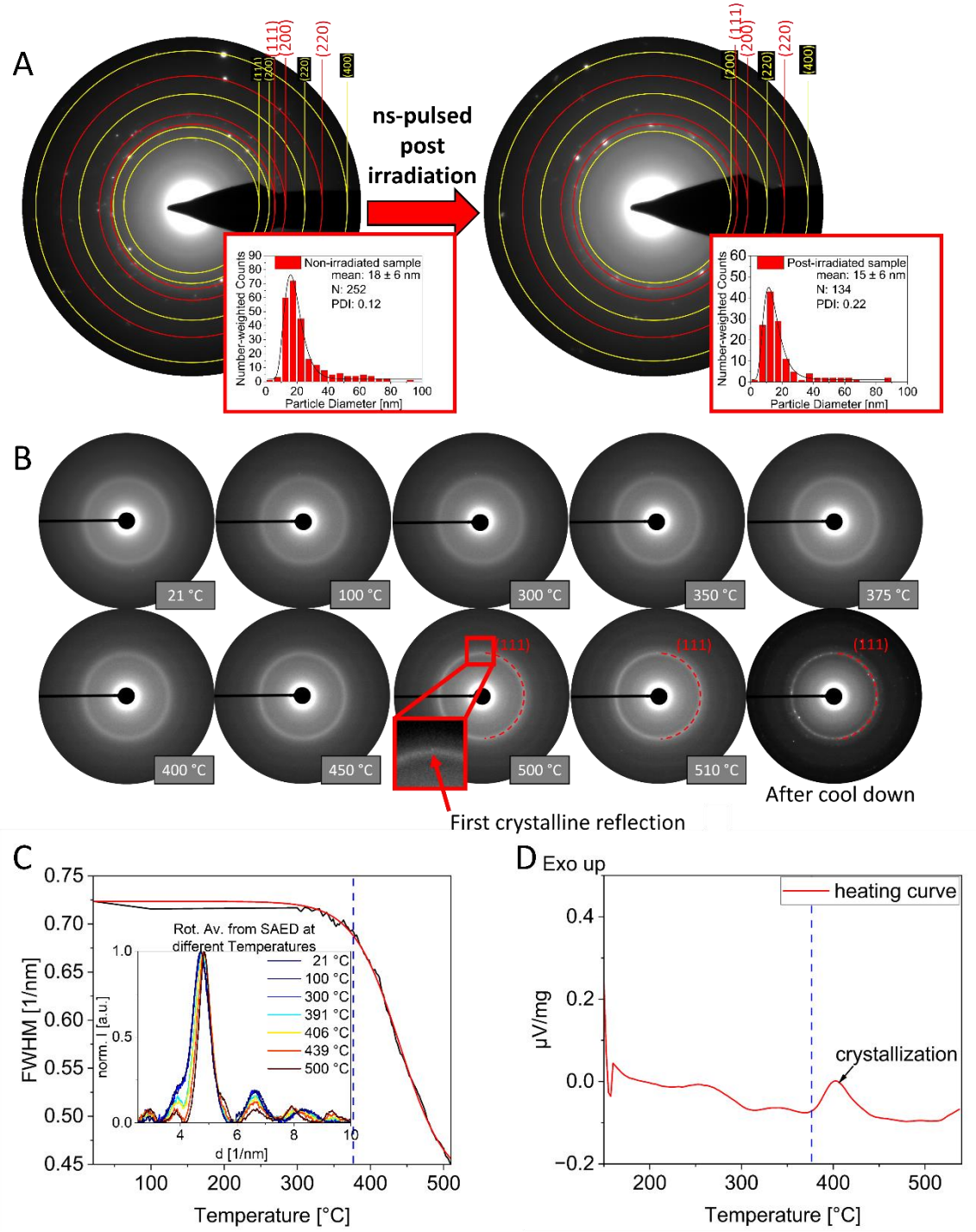

Figure 4: (A) Post-irradiation experiment of a colloid obtained by ps-LAL (left), showing both the SAED pattern and particle size distribution, and the colloid obtained after irradiation with ns-pulses (right) with no decrease in crystallinity and no significant difference in the particle size distribution. Here, reflections displayed in red are assigned to the fcc phase whereas reflections marked with yellow circles are derived from metal oxides. (B) *In situ* TEM heating experiment of amorphous HEA NPs by ns-

LAL, depicting SAED pattern in different temperature steps with a first reflection ((111)-fcc) at 500 °C. After cooling down, a significant intensity of reflections is detectable. (C) FWHM of the (111)-fcc rings (derived from rotational average) in the SAED patterns of the heating experiment show a significant decrease starting at around 375 °C, underlining the starting crystallization of the amorphous particles. The black line shows raw data and the red line represents a Boltzmann fit. (D) DSC heating profile of the amorphous HEA NPs obtained by ns-LAL shows the exothermic crystallization process that begins at 375 °C, complementing the heating experiments and the analysis of the FWHM.

Thermal stability of the amorphous HEA nanoparticles

Finally, we aimed to examine the temperature-stable the amorphous HEA NPs. Thereto, we conducted *in situ* heating experiments in TEM as well as differential scanning calorimetry. Figure 4B displays the TEM *in situ* heating experiment and SAED patterns of an amorphous sample made by ns-LAL in acetone with increasing temperature. The diffuse and broad intensity that results from an amorphous structure gets sharper, especially for the (111)-ring, meaning that the energy input by heating results in the formation of crystallites that grow with increasing temperatures. At 500 °C the first weak reflection appears, with a d-value of 2,1 Å that belongs to the (111)-face of the fcc-structure (compare with Figures 1A and 2A). These reflections get more pronounced after cooling down which can be attributed to enhanced Bragg diffraction at lower temperatures while crystallite growth after particle cooldown could also be possible. This is consistent with the heating providing the activation energy for the initiation of this process followed by spontaneous transformation into the thermodynamically favored crystalline state. In addition, we observe a decrease of the

full width at half-maximum (FWHM, derived by rotational average from SAED analysis) of the investigated (111)-ring in the *in situ* heating experiment (Figure 4C), which indicates the formation of larger crystallites in SAED. As shown in the DSC measurement in Figure 4D, the crystallization of the amorphous particles is an exothermic process and begins at approximately 375 °C which is exactly the same temperature where the rapid decrease of the FWHM in Figure 4C starts and the required thermal energy k_BT is achieved to overcome the activation energy. Note that for the determination of the plot in Figure 4C more temperature steps were considered than shown in Figure 4B, however, due to clarity reasons the full data set of 94 SAED patterns is not shown and can be found in the supplementary information as a video file. The observation of amorphous particles transforming into a crystalline phase validates that the amorphous phase is metastable whereas the crystalline structure is the thermodynamic favored one [78, 79]. Furthermore, it shows that the amorphous HEA NPs are structurally temperature stable, which could be advantageous in harsh applications like the thermal conditions of catalysis or magnetic applications.

Mechanistic Discussion

Based on these findings we can conclude that the crystal structure of these HEA NPs is pre-determined directly during particle formation, probably in the ablation plume phase. Previous studies investigated the LAL process using a picosecond-pulsed laser in comparison to a nanosecond-pulsed laser [40, 55, 72]. As stated in these works, ps-LAL leads to more vigorous ablation conditions (up to 12 000 K maximum temperature and peak pressures of up to 38 GPa), related to the conditions of stress and thermal confinement of the deposited laser energy. Contrary, in ns-LAL the energy of the laser pulse is transferred deeper into the bulk target, even though peak temperature and pressure is significantly lower (~ 5000 – 8000 K and 4.8 GPa). Note that those

numbers result from a computational model of pure silver in water for ps-LAL and ns-LAL so transferability to HEA NPs in organic solvents may be limited. Also, the longest calculated pulse in Ref. [55] has a length of 2 ns, whereas in this work the pulse duration is 10 ns in the case of ns-LAL, possibly leading to conditions that may be even more dictated by thermal processes. Consequently, we can expect a longer heating of the plume in our experiments than observed in the simulated study and thus longer heated periods during the early phase of LAL. Although the aforementioned studies describe different processes that happen during LAL with different pulse durations, the factor with the most pronounced impact on amorphization in this context is the particle cooling rate. However, the cooling rates during ps-LAL and ns-LAL are estimated to be both high enough to initiate amorphization but are also in a comparable regime with rates of 10^{12} K/s – 10^{13} K/s in both cases [40, 55]. Based on this we can conclude that the pronounced differences in amorphization during ps-LAL and ns-LAL are not caused by differences in cooling rate, but the different plume heating times during LAL. Moreover, the heating duration alone is unlikely the only prerequisite for amorphization, but also the different intensity and/or duration of chemical reactions of the plume with the solvent.

One difference between LAL with ps and ns pulses is that ns-LAL goes along with a more pronounced melting of the target surface (higher thermal penetration depth and lateral heating), compared to ps-LAL, a process that Waag et al. described experimentally by comparing target surfaces after both ps- and ns-LAL [80]. This is because in ns-LAL, thermal processes overweigh and thus, the ablation process is not as vigorous as in ps-LAL. Further, due to the longer exposure of thermal penetration in ns-LAL, the ablation plume tends to be heated for a longer time compared to ps-LAL. However, in both ns- and ps-laser ablation in organic solvents, active carbon species (radicals, permanent gases, degradation and condensation products as well

as elemental carbon) form [44, 81, 82]. These carbon species can interact with the plume and diffuse into the nanoparticles, depending on the affinity of nanoparticle constituting elements to carbon or carbon solubility [33, 83, 84]. Note that the degradation of solvent molecules is even higher for ps-LAL than for ns-LAL [44], meaning that the resulting structural differences in HEA NPs do not occur due to a higher availability of carbon. Diffusing carbon into a metallic matrix has been reported before for monometallic systems [83, 85, 86] and alloys [67, 68], stabilizing amorphous structures and enhancing glass formation ability (GFA). In general, Si, B, P, and carbon have been reported to diffuse into metallic matrixes and thus enhance the GFA, whereas carbon seems to have the biggest effect on GFA [86], thus, resulting in an amorphous structure with short-range order [66]. As ns-LAL keeps thermal plume heating orders of magnitude longer in play, we hypothesize that the organic solvent molecules and the formed carbon species may react longer at the plume front, in particular the mixing region where the ablated matter interpenetrates the solvent vapor. In that region, the nanoparticle droplets stemming from the plume cool fast and solidify first [40]. Thus, the carbon species will have more time to interact with the plume and diffuse more significantly into the metallic matrix of the forming HEA NPs, being the reason behind the stabilized amorphous structure. In other words, compared to ps-LAL, during ns-LAL the extended heating times allow enhanced carbon diffusion into the metallic matrix. Figure 5 illustrates the hypothesized differences during ps- and ns-LAL. In ps-LAL, the time when the temperature is high enough for the plume and particles to stay in a liquid state (T_L) is short and can be expected to be only a few ns (pulse duration of 10 ps and additional heated period [40]). The molten particle that is surrounded by reactive carbon species (Figure 5 (1)) is cooled down rapidly by heat exchange with the solvent and experiences a fast transition down to temperatures that are low enough for undercooling and solidification (T_S) (Figure 5 (2)) whereas the

carbon (if a carbon shell is available) rather stays on the surface of the particle. Consequently, the HEA NPs are formed in crystalline nature (single- or polycrystalline, often with defects) with potential carbon species on their surfaces (e.g. graphitic carbon shells) (Figure 5 (3) and (4)). In contrast, during ns-LAL the conditions of T_L are present for a longer time period and thereby the plume and alloy droplets are expected to stay in these conditions for approximately 15 ns (pulse duration of 10 ns and additional heated period [55]). Consequently, the emerging liquid nanoparticles (Figure 5 (5)) are in a liquid state for a longer time and thus active carbon species can diffuse more significantly into the molten metal core of the nanoparticles (Figure 5 (6)), although a part of that can also stay on the outside of the particle (Figure 5 (7)), depending on the thermal history of the individual particle. In this case, the carbon is present in both the resolidifying metal core and on the surface of the particle. Therefore, after cooldown and transition into T_S, a crystalline structure is inhibited due to the present carbon, stabilizing the amorphous structure of the HEA NP (Figure 5 (8)).

Looking at the diffusing carbon atoms during the period of T_L, we additionally calculated the mean square displacements (MSD) of diffusing carbon atoms by using diffusion coefficients of carbon in FeNi at high temperatures and high pressures as reported by Lin et al. [87]. Using the estimated durations of 15 ns for ns-LAL and 2 ns for ps-LAL, the MSD falls within the one-digit nanometer range for both cases, though the value for ns-LAL is three times higher than for ps-LAL. Notably, the diffusion coefficients reported by Lin et al. were studied under conditions that come closer to ns-LAL than ps-LAL (regarding temperature and pressure). Since diffusion coefficients are inversely proportional to pressure and directly proportional to temperature, it is important to note that the pressure in ps-LAL can be ten times higher than in ns-LAL while the temperature is only around twice as high. Consequently, we can expect that the MSD is even lower for ps-LAL, possibly falling in a sub-nanometer range, which makes

diffusion into liquid metal droplets more unlikely. This hypothesized mechanism that takes carbon diffusion into the particle´s core into account extends the earlier stated assumption that amorphization is a result of a not-yet-crystallized structure that is stabilized by carbon shells throughout the cooling process [54]. Also, note that the aforementioned cooling rates of 10^{12} – 10^{13} K/s are crucial for preserving the amorphous structure as lower cooling rates would lead to the precipitation of carbon species to the particles´ surface which was discussed by Abdelhafiz et al. in the context of high-entropy oxide materials via CTS [88]. Of course, carbon diffusion into the particle core after its cooldown may not be excluded and can even happen at room temperature, but this is unlikely to be the driving factor as this may not explain the differences in the nanoparticle structure caused by ps- or ns-LAL that create particles of similar size. Also, note that the estimated durations of T_L refer to simulations on silver so the durations for the Cantor alloy may differ because of lower thermal conductivity [89, 90] and different electron-phonon-coupling strength.

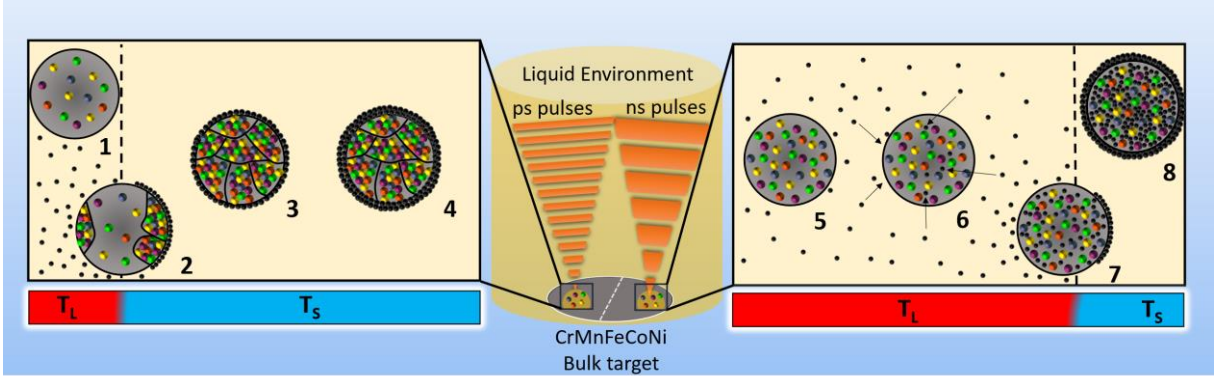

Figure 5: How the particle structure is set by laser pulse duration: Graphical illustration of the hypothesized mechanism behind the pulse-dependent structure of CrMnFeCoNi HEA NPs by ns- and ps-LAL in organic liquids, stating the interplay between metallic atoms (colored spheres) and active carbon species (black spheres). In the center, the bulk material is ablated by either nanosecond or picosecond pulses in liquid (liquid is illustrated by yellow cylinder). During picosecond LAL, after the energy transfer into

the bulk target, the plume with liquid nanodroplets forms (at liquid-state temperatures, T_L), surrounded by active carbon species (1). Solidification temperatures (T_S) are reached rapidly (2) which yields (poly)crystalline particles with carbon shells (3) that possibly can grow due to post-condensation processes (4) (similar post-condensation mechanisms were also postulated and discussed by Fromme et al. in reference [82]). Contrary, during nanosecond LAL, the period of T_L lasts significantly longer as the energy from the pulse is pumped into the plume three orders of magnitude longer. Consequently, the particles stemming from the plume that is in a liquid state (5) can be doped more intensively by diffusing carbon into the molten metal core (6 and 7). After solidification, the NPs cannot form proper crystallites with the expected fcc structure, but form C-doped amorphous structures, analogously surrounded by carbon shells as well (8).

Conclusion

Understanding the structure formation determinants of high entropy alloy nanoparticles is a prerequisite in further development of nanomaterial fabrication methods for application in heterogeneous catalysis and magnetism. Laser synthesis of colloids is a scalable nanofabrication method that provides kinetic control over the structural formation of nanoparticles because of the high cooling rates. On the other hand, less is known about the interplay with the liquid, in particular organic liquid where the solvent molecule may deliver active carbon species that may form carbon shells or even act as carbon dopant to nanoparticle cores of complex compositional alloys. We examined the primary factors influencing the metallic glass formation (amorphization) in the quinary precious metal-free Cantor system (CrMnFeCoNi), synthesized by pulsed laser ablation in liquid. We found that the main determinant for the GFA during

synthesis is the laser pulse duration, with ps pulses favoring crystalline structures and ns pulses triggering amorphization due to proposed carbon diffusion into the forming HEA NPs. Thereby, potential influencing factors such as organic solvent type, particle size, target surface properties, nanoparticle composition, post-irradiation effects, and laser fluence were systematically excluded, leaving the determinant of pulse duration as the ruling factor in the structural difference.

We further confirmed that the amorphous structure is metastable by conducting *in situ* heating and DSC experiments, showing that phase transformation from amorphous to crystalline can be achieved by heating particles above 375 °C. This outstanding temperature stability renders those nanosecond-laser-made particles to be interesting candidates for thermal catalysis or magnetic devices that pose high demand of structural robustness against heat.

This study advances the understanding of high-entropy alloy (or compositionally complex solid solutions) nanoparticles synthesized via laser ablation in organic liquids, highlighting how pulse duration sets structural differences. Technically, the switching between crystalline or amorphous nanoparticle outflow may easily be implementable, simply by switching a mirror that guides either a ps or ns pulsed laser beam into the ablation chamber. These findings are valuable for researchers in the field of laser-synthesized nanomaterials and the extension to other multi-element alloy systems would be of interest, enhancing knowledge of laser-based synthesis of (high-entropy alloy) nanoparticles. In this context, it would be interesting to examine further whether or to what extent amorphization tendencies are linked to the carbon affinity of individual elements in the alloy. Additionally, the application potential of metallic glass nanoparticles is high, such as high intrinsic activity in both electrocatalysis and heterogeneous catalysis, where their disordered atomic structure provides a high density of active sites, which enhances their catalytic performance. Furthermore, in the

field of energy storage devices, like batteries and supercapacitors, such amorphous nanoparticles are interesting materials. Here, the combination of complex composition based on the HEA concept with carbon doping elevating the Cantor composition´s glass-forming ability could be an interesting playground, in particular as i) the formed particles have outstanding temperature stability, and ii) the LAL is a fabrication method with well-documented scalability and robustness.

Experimental

HEA Nanoparticle Synthesis

For HEA NP synthesis, the corresponding ablation target with a nominal composition of $Cr_{20}Mn_{20}Fe_{20}Co_{20}Ni_{20}$ was produced by weighing and heat-treating metal granules of Cr, Mn, Fe, Co Ni (Evochem, purity 99.95 – 99.99 %) inside an arc-melting oven in an argon atmosphere for melting and sintering. The inert atmosphere was used to avoid oxidation of the ignoble metals used. The sintered target was remelted three times to ensure homogeneity and uniform phase formation.

The ligand-free HEA NPs were LAL-synthesized in acetone, ethanol, and acetonitrile (VWR, purity ≥ 99.8 %). Before ablation, the bulk target was polished with sandpaper to ensure it was free of surface oxides. All commercially available analytical grade solvents (purity ≥ 99.8 %) were purified by dewatering (molecular sieve 4 Å, Carl Roth), distillation, and subsequent degassing with argon to minimize contamination and oxidation of the HEA NPs. The ablation was conducted in a self-designed stirred batch reactor with a volume of 30 mL using an Nd:YAG laser (Ekspla, Atlantic Series, 10 ps, 1064 nm, 100 kHz, 0.15 mJ) for ps-LAL and a nanosecond Laser (Rofin, Powerline E20, 10 ns, 1064 nm, 10 kHz, 0.50 mJ) for ns-LAL. Ablation was conducted for 5 minutes. The laser beam was moved on the target with a galvanometric scanner

(100 mm focal length) in a spiral pattern, while lateral inter-pulse distances were set to avoid interactions between the cavitation bubbles and consecutive pulses.

Table 1: Overview of the pulsed lasers used in this work with all relevant system parameters.

Laser	**Picosecond**	**Nanosecond**
Pulse duration	10 ps	10 ns
Wavelength	1064 nm	1064 nm
Repitation rate	100 kHz	10 kHz
Pulse energy	0.15 mJ	0.50 mJ

For evaluation and application of laser fluences, a Baumer USB-camera was used with the help of Laser Light Inspector software, applying a Gaussian fit and using the $1/e^2$ method to determine laser beam diameters. For laser power, a power meter (PowerMax PM30, Coherent) was used, measuring the average laser power behind all optics.

Post-irradiation control experiments were conducted in standard quartz glass cuvettes (Hellma Analytics, High Precision Cell) with a colloid volume of 3 mL. Focusing conditions and irradiated volumes in the cuvette closely mimicking those in the ablation chamber were realized (Figure S1). The colloids, whether made by ps-LAL or ns-LAL, were irradiated in a colloidal state by the respective lasers. This allowed us to emulate and investigate the contribution of the by-process of post-irradiation of colloids in the liquid volume in front of the ablation target during LAL.

Material Characterization Methods

Target characterization was conducted by X-ray powder diffraction (XRD, Bruker D8 Advance, Cu Kα with $\lambda = 1.54$ Å) in reflection mode in a 2θ range 5 to 130° with a step

size of 0.01° and a counting time of 1.2 s, scanning electron microscopy with energy dispersive spectroscopy (SEM-EDS, Philips XL30 with EDAX system) analysis as well as X-ray fluorescence spectroscopy (XRF, S8 Tiger, Bruker) to confirm global composition, elemental distribution and crystal structure. HEA NPs were characterized via XRD by drying drop cast, whereby concentrated colloidal HEA NPs with comparable masses were placed on Si single-crystal sample holder to minimize scattering. The measurements were performed with the same diffractometer (Bruker D8 Advance) in a 2θ range of 20 to 90° with a step size of 0.02° and a counting time of 8 s. For the qualitative phase analysis, the Bruker software Diffrac Suite EVA V7.1 was used with the face-centered cubic Ni (#70-1849) and MnO (#75-0257) pattern from the ICDD database. To calculate the lattice parameters and the average crystallite size, a quantitative Rietveld refinement was performed with the Bruker software TOPAS 7.0, after the instrumental characterization with a microcrystalline powder LaB6 (SRM 660b of NIST, a = 4.15689 Å) was done.

TEM analysis including selected area electron diffraction (SAED, d-value determination errors within ± 0.01 Å range) and high-resolution TEM (HRTEM) was performed using a Tecnai F30 STwin G2 (300 kV acceleration voltage) equipped with a Si(Li) detector (EDAX system) and a JEOL JEM 2100 (200 kV acceleration voltage). Chemical analysis involving elemental mapping and line scanning was conducted at a probed-corrected JEOL JEM-ARM200F NEOARM scanning transmission electron microscope operated at 200 kV (cold-FEG) using energy-dispersive X-ray spectroscopy (EDS) with a dual silicon drift detector system with 100 mm2 active area each. Additionally, *in situ* heating experiments were performed utilizing TEM and SAED also at the same JEOL NEOARM provided with a Lightning HB+JEOL holder from DENS solutions. All samples for TEM analysis were prepared by drop-casting the NP colloid on copper grids with a lacey carbon film (Plano GmbH) or silicon nitride films

(TED Pella Inc. 35 nm, 70x70 µm aperture). For *in situ* heating experiments a wildfire Nano-Chip GT from DENS solutions was used as a substrate. After drop-casting all samples were dried in the atmosphere using an infrared lamp (Philips Infrared PAP38E, 150W) for 1 min and permanently stored under vacuum to avoid further contamination and oxidation.

Differential scanning calorimetry (DSC) was conducted on the 204 Cell (Netzsch) with a heating rate of 1 K/min and $MnCl_3$ as reference material to determine phase transitions in amorphous high-entropy alloy nanoparticles. To avoid unwanted processes, an inert atmosphere was created by flushing the measurement chamber with argon gas.

Acknowledgements

The authors gratefully thank Jurij Jakobi for his experimental and analytical support and Florian de Kock for preparation of the bulk material used in this work.

Funding

The authors thank the Deutsche Forschungsgemeinschaft (DFG) for financial support within the project Nr. 277627168.

References

1. Löffler, T.; Ludwig, A.; Rossmeisl, W.; Schuhmann, W. *Angew. Chem., Int. Ed.,* **2021,** *60,* 26894–26903.

2. Han, L.; Zhu, S.; Rao, Z.; Scheu, C.; Ponge, D.; Ludwig, A.; Zhang, H.; Gutfleisch, O.; Hahn, H.; Li, Z.; Raabe, D. *Nat. Rev. Mater.*, **2024,** 9, 846–865.

3. Rao, Z.; Tung, P.; Xie, R.; Wei, Y.; Zhang, H.; Ferrari, A.; Klaver, T.; Körmann, F.; Sukumar, P. T.; Kwiatkowski da Silva, A.; Chen, Y.; Li, Z.; Ponge, D.; Neugebauer, J.; Gutfleisch, O.; Bauer, S.; Raabe, D. *Science*, **2022,** 378, 78-85.

4. Xie, P.; Yao, Y.; Huang, Z.; Liu, Z.; Zhang, J.; Li, T.; Wang, G.; Shahbazian-yassar, R.; Hu, L.; Wang, C.; *Nat. Commun.*, **2019**, 10, 4011.

5. Wilsey, M. K.; Cox, C. P.; Forsythe, R. C.; McCarney, L. R.; Müller, A. M. *Catal. Sci. Technol.*, **2021,** 11, 416-424.

6. Liu, Y.; Chen, Z.; Yang, X.; Zhang, J.; Sun, Z.; Chen, Y.; Liu, F. *J. Mater. Res. Technol.,* **2021,** 15, 256-267.

7. Feng, Y.; Yao, H.; Sun, Z.; Liao, Y.; Wang, J.; Zhao, R.; Li, Y. *ACS Appl. Mater. Interfaces*, **2024,** 16, 41027-41035.

8. Li, H.; Han, Y.; Zhao, H.; Qi, W.; Zhang, D.; Yu, Y.; Cai, W.; Li, S.; Lai, J.; Huang, B.; Wang, L.; *Nat. Commun.*, **2020,** 11, 5437.

9. Rawat, R.; Singh, B. K.; Tiwari, A.; Arun, N.; Pathak, A. P.; Shadangi, Y.; Mukhopadhyay, N. K.; Nelamarri, S. R.; Rao, S. V.; Tripathi, A. *J. Alloys Compd.*, **2022,** 927, 166905.

10. Li, Y.; Liao, Y.; Ji, L.; Hu, C.; Zhang, Z.; Zhang, Z.; Zhao, R.; Rong, H.; Qin, G.; Zhang, X. *Small*, **2022**, 18, 2107265.

11. Dąbrowa, J.; Zajusz, M.; Kucza, W.; Cieślak, G.; Berent, K.; Czeppe, T.; Kulik, T.; Danielewski, M. *J. Alloys Compd.*, **2019**, 783, 193-207.

12. Pickering, E. J.; Jones, N. G. *Int. Mater. Rev.*, **2016,** 61, 183-202.

13. Zhang, P., Hui, X.; Nie, Y.; Wang, R.; Wang, C.; Zhang, Z.; Yin, L. *Small*, **2023,** 19, 2206742.

14. Jin, Z.; Lv, J.; Jia, H.; Liu, W.; Li, H.; Chen, Z.; Lin, X.; Xie, G.; Liu, X.; Sun, S.; Qiu, H.-J. *Small*, **2019,** 15, 1904180.

15. Batchelor, T. A.; Pedersen, J. K.; Winther, S. H.; Castelli, I. E.; Jacobsen, K. W.; Rossmeisl, J. *Joule*, **2019,** 3, 834-845.

16. Qiu, H.-J.; Fang, G.; Wen, Y.; Liu P.; Xie, G.; Liu, X.; Sun, S. *J. Mater. Chem.*, **2019,** 7, 6499-6506.

17. Pedersen, J. K.; Batchelor, T. A. A.; Bagger, A.; Rossmeisl, J. *ACS Catal.*, **2020,** 10, 2169-2176.

18. Löffler, T.; Waag, F.; Gökce, B.; Ludwig, A.; Barcikowski, S.; Schuhmann, W. *ACS Catal.*, **2021,** 11, 1014-1023.

19. Luan, C.; Escalera-Lopez, D.; Hagemann, U.; Kostka, A.; Laplanche, G.; Wu, D.; Cherevko, S.; Li, T. *ACS Catal.*, **2024,** 14, 12704-12716.

20. Yao, Y.; Huang, Z.; Xie, P.; Lacey, S. D.; Jacob, R. J.; Xie, H.; Chen, F.; Nie, A.; Pu, T.; Rehwoldt, M.; Yu, D.; Zachariah, M. R.; Wang, C.; Shahbazian-yassar, R.; Li, J.; Hu, L. *Science*, **2018,** 359, 1489-1494.

21. Geng, M.; Zhu, Y.; Guan, J.; Zhang, R.; Zou, Q.; Wang, L.; Guo, B.; Zhang, M. *J. Alloys Compd.*, **2024,** 1005, 176180.

22. Huang, X.; Wu, Z.; Zhang, B.; Yang, G.; Wang, H.-F.; Wang, H.; Cao, Y.; Peng, F.; Li, S.; Yu, H. *Small*, **2024,** 20, 2311631.

23. Kar, N.; McCoy, M.; Wolfe, J.; Bueno, S. L. A.; Shafei, I. H.; Skrabalak, S. E. *Nat. Synth.*, **2024,** 3, 175-184.

24. Gao, S.; Hao, S.; Huang, Z.; Yuan, Y.; Han, S.; Lei, L.; Zhang, X.; Shahbazian-yassar, R.; Lu, J. *Nat. Commun.*, **2020,** 11, 2016.

25. Wu, D.; Kusada, K.; Yamamoto, T.; Toriyama, T.; Matsumura, S.; Kawaguchi, S.; Kubota, Y.; Kitagawa, H. *J. Am. Chem. Soc.*, **2020**, 142, 13833-13838.

26. Wan, W.; Liang, K.; Zhu, P.; He, P.; Zhang, S. *J. Mater. Sci. Technol.*, **2024**, 178, 226-246.

27. Li, K.; Chen, W. *Mater. Today Energy.*, **2021**, 20, 100638.

28. Sun, X.; Sun, Y. *Chem. Soc. Rev.*, **2024**, 53, 4400-4433.

29. Ritter, T. G.; Pappu, S.; Shabazian-Yassar, R. *Adv. Energ. Sust. Res.*, **2024,** 5, 2300297.

30. Ma, Y.; Jiang, B.; Li, C.; Wang, Q.; Dong, C.; Liaw, P.; Xu, F.; Sun, L. *Metals*, **2017,** 7, 57.

31. Zhou, X.; Zhu, H.; Fu, S.; Lan, S.; Hahn, H.; Zeng, J.; Feng, T. *Small,* **2024**, e2405596.

32. Dvurečenskij, A.; Cigáň, A.; Lobotka, P.; Radnóczi, G.; Škrátek, M.; Benyó, J.; Kováčová, E.; Majerová, M.; Maňka, J. *J. Alloys Compd.,* **2022**, *896*, 163089.

33. Reichenberger, S.; Marzun, G.; Muhler, M.; Barcikowski, S. *ChemCatChem,* **2019**, *11*, 4489–4518.

34. Zhang, D.; Gökce, B.; Barcikowski, S. *Chemical reviews,* **2017**, *117*, 3990–4103.

35. Forsythe, R. C.; Cox, C. P.; Wilsey, M. K.; Müller, A. M. *Chem. Rev.* **2021**, *121*, 7568–7637.

36. Manshina, A. A.; Tumkin, I. I.; Khairullina, E. M.; Mizoshiri, M.; Ostendorf, A.; Kulinich, S. A.; Makarov, S.; Kuchmizhak, A. A.; Gurevich, E. L. *Adv. Funct. Mater.* **2024**, *34*, 2405457.

37. Zhang, D.; Liu, J.; Li, P.; Tian, Z.; Liang, C. *ChemNanoMat,* **2017**, *3*, 512–533.

38. Waag, F.; Streubel, R.; Gökce, B.; Barcikowski, S. *Appl Nanosci.,* **2021**, *11*, 1303–1312.

39. Streubel, R.; Barcikowski, S.; Gökce, B. *Opt. Lett.,* **2016**, *41*, 1486–1489.

40. Chen, C.; Zhigilei, L. V. *Appl. Phys. A,* **2023**, *129*, 1–35.

41. Zeng, H.; Du, X.-W.; Singh, S. C.; Kulinich, S. A.; Yang, S.; He, J.; Cai, W. *Adv. Funct. Mater.,* **2012**, *22*, 1333–1353.

42. Yogesh, G. K.; Shukla, S.; Sastikumar, D.; Koinkar, P. *Appl. Phys. A,* **2021**, *127*, 1–40.

43. Fazio, E.; Gökce, B.; Giacomo, A. de; Meneghetti, M.; Compagnini, G.; Tommasini, M.; Waag, F.; Lucotti, A.; Zanchi, C. G.; Ossi, P. M. *Nanomater.,* **2020**, *10*, 2317.

44. Fromme, T.; Reichenberger, S.; Tibbetts, K. M.; Barcikowski, S. *Beilstein J. Nanotechnol.* **2024**, *15*, 638–663.

45. Amendola, V.; Amans, D.; Ishikawa, Y.; Koshizaki, N.; Scirè, S.; Compagnini, G.; Reichenberger, S.; Barcikowski, S. *Chem. Eur. J.,* **2020**, *26*, 9206–9242.

46. Ziefuß, A. R.; Reichenberger, S.; Rehbock, C.; Chakraborty, I.; Gharib, M.; Parak, W. J.; Barcikowski, S. *J. Phys. Chem. C,* **2018**, *122*, 22125–22136.

47. Havelka, O.; Cvek, M.; Urbánek, M.; Łukowiec, D.; Jašíková, D.; Kotek, M.; Černík, M.; Amendola, V.; Torres-Mendieta, R. *Nanomater.,* **2021**, *11*, 1538.

48. Frias Batista, L. M.; Kunzler, K.; John, M. G.; Clark, B.; Bullock, A.; Ferri, J.; Gupton, B. F.; Tibbetts, K. M. *Appll Surf. Sci.,* **2021**, *557*, 149811.

49. Nag, A.; Nguyen, C. M.; Tibbetts, K. M. *Appl. Surf. Sci.,* **2023**, *610*, 155384.

50. Nakamura, T.; Magara, H.; Herbani, Y.; Sato, S. *Appl. Phys. A,* **2011**, *104*, 1021–1024.

51. Waag, F.; Li, Y.; Ziefuß, A. R.; Bertin, E.; Kamp, M.; Duppel, V.; Marzun, G.; Kienle, L.; Barcikowski, S.; Gökce, B. *RSC Adv.,* **2019**, *9*, 18547–18558.

52. Wang, B.; Wang, C.; Yu, X.; Cao, Y.; Gao, L.; Wu, C.; Yao, Y.; Lin, Z.; Zou, Z. *Nat. Synth.,* **2022**, *1*, 138–146.

53. Tahir, S.; Shkodich, N.; Eggert, B.; Lill, J.; Gatsa, O.; Flimelová, M.; Adabifiroozjaei, E.; Bulgakova, N. M.; Molina-Luna, L.; Wende, H. *ChemNanoMat.*, **2024,** 10, e202400064.

54. Johny, J.; Li, Y.; Kamp, M.; Prymak, O.; Liang, S.-X.; Krekeler, T.; Ritter, M.; Kienle, L.; Rehbock, C.; Barcikowski, S. *Nano Res.,* **2022**, *15*, 4807–4819.

55. Shih, C.-Y.; Shugaev, M. V.; Wu, C.; Zhigilei, L. V. *Phys. Chem. Chem. Phys.,* **2020**, *22*, 7077–7099.

56. Huang, H.; Zhigilei, L. V. *J. Phys. Chem. C,* **2021**, *125*, 13413–13432.

57. Huang, W.; Johnston-peck, A. C.; Wolter, T.; Yang, W. D.; Xu, L.; Oh, J.; Reeves, B. A.; Zhou, C.; Holtz, M. E.; Herzing, A. *Science*, **2021,** 378, 1518-1523.

58. Li, Z.; Fu, J.-Y.; Feng, Y.; Dong, C.-K.; Liu, H.; Du, X.-W. *Nat. Catal.,* **2019**, *2*, 1107–1114.

59. Johny, J.; Kamp, M.; Prymak, O.; Tymoczko, A.; Wiedwald, U.; Rehbock, C.; Schürmann, U.; Popescu, R.; Gerthsen, D.; Kienle, L.; Shaji, S.; Barcikowski, S. *J. Phys. Chem. C,* **2021**, *125*, 9534–9549.

60. Kamp, M.; Tymoczko, A.; Schürmann, U.; Jakobi, J.; Rehbock, C.; Rätzke, K.; Barcikowski, S.; Kienle, L. *Cryst. Growth Des.,* **2018**, *18*, 5434–5440.

61. Glasscott, M. W.; Pendergast, A. D.; Goines, S.; Bishop, A. R.; Hoang, A. T.; Renault, C.; Dick, J. E. *Nat. Commun.,* **2019**, *10*, 2650.

62. Deng, B.; Wang, Z.; Choi, C. H.; Li, G.; Yuan, Z.; Chen, J.; Luong, D. X.; Eddy, L.; Shin, B.; Lathem, A.; Chen, W.; Cheng, Y.; Xu, S.; Liu, Q.; Han, Y.; Yakobson, B. L.; Zhao, Y.; Tour, J. M. *Adv. Mater.,* **2024**, *36*, e2309956.

63. Wachter, J.; Amigo, N.; Gutiérrez, G.; Zúñiga, A. *J. Non-Cryst. Solid,* **2024**, *628*, 122866.

64. Louzguine-Luzgin, D. V.; Pratama, F. R. *Intermetallics,* **2024**, *164*, 108120.

65. Zhu, Y.; Wang, H.; Wu, L.; Li, M. *Appl. Phys. Lett.,* **2023**, *123.*

66. Liang, S.-X.; Zhang, L.-C.; Reichenberger, S.; Barcikowski, S. *Phys. Chem chem. Phys.,* **2021**, *23*, 11121–11154.

67. Liang, S.-X.; Reusmann, M. E.; Loza, K.; Zerebecki, S.; Zhang, L.-C.; Jia, Z.; Reichenberger, S. *Mater. Today Chem.,* **2023**, *30*, 101544.

68. Liang, S.-X.; Salamon, S.; Zerebecki, S.; Zhang, L.-C.; Jia, Z.; Wende, H.; Reichenberger, S.; Barcikowski, S. *Scr. Mater.,* **2021**, *203*, 114094.

69. Su, Z.; Zhang, C.; Liu, J.; Liang, C. *J. Electroanal. Chem.,* **2024**, *960*, 118182.

70. Marzun, G.; Bönnemann, H.; Lehmann, C.; Spliethoff, B.; Weidenthaler, C.; Barcikowski, S. *ChemPhysChem.,* **2017**, *18*, 1175–1184.

71. Vorontsov, A. V.; Tsybulya, S. V. *Ind. Eng. Chem. Res.,* **2018**, *57*, 2526–2536.

72. Shih, C.-Y.; Streubel, R.; Heberle, J.; Letzel, A.; Shugaev, M. V.; Wu, C.; Schmidt, M.; Gökce, B.; Barcikowski, S.; Zhigilei, L. V. *Nanoscale,* **2018**, *10*, 6900–6910.

73. Bhattacharjee, P. P.; Sathiaraj, G. D.; Zaid, M.; Gatti, J. R.; Lee, C.; Tsai, C.-W.; Yeh, J.-W. *J. Alloys. Compd.,* **2014**, *587*, 544–552.

74. Honig, R. E. Vapor pressure data for the solid and liquid elements. *RCA Rev.,* **1969**, *30*, 285–305.

75. Web of Elements. https://www.webelements.com (accessed January 30, 2025).

76. Redka, D.; Winter, J.; Gadelmeier, C.; Djuranovic, A.; Glatzel, U.; Minár, J.; Huber, H. P. *Appl. Surf. Sci.,* **2022**, *594*, 153427.

77. Menéndez-Manjón, A.; Schwenke, A.; Steinke, T.; Meyer, M.; Giese, U.; Wagener, P.; Barcikowski, S. *Appl. Phys. A,* **2013**, *110*, 343–350.

78. Sun, J.; Sinha, S. K.; Khammari, A.; Picher, M.; Terrones, M.; Banhart, F. *Carbon,* **2020**, *161*, 495–501.

79. Yeghishyan, A.; Malakpour Estalaki, S.; Chilukuri, R.; Zakaryan, M. K.; Luo, T.; Manukyan, K. *J. Phys. Chem. C*, **2024**, *128*, 11456–11464.

80. Waag, F.; Fares, Wessam I. M. A.; Li, Y.; Andronescu, C.; Gökce, B.; Barcikowski, S. *J. Mater. Sci.,* **2022**, *57*, 3041–3056.

81. Fromme, T.; Tintrop, L. K.; Reichenberger, S.; Schmidt, T. C.; Barcikowski, S. *ChemPhysChem.,* **2023**, *24*, e202300089.

82. Fromme, T.; Müller, R.; Krenz, L.; Tintrop, L. K.; Sanjuán, I.; Schmidt, T. C.; Tibbetts, K. M.; Andronescu, C.; Reichenberger, S.; Barcikowski, S. *J. Phys. Chem. C*., in press.

83. Zhang, H.; Liang, C.; Liu, J.; Tian, Z.; Shao, G. T. *Carbon,* **2013**, *55*, 108–115.

84. Jung, H. J.; Choi, M. Y. *Appl. Surf. Sci.,* **2018**, *457*, 1050–1056.

85. Zhang, D.; Zhang, C.; Liu, J.; Chen, Q.; Zhu, X.; Liang, C. *ACS Appl. Nano Mater.,* **2019**, *2*, 28–39.

86. Wu, Y.; Hui, X. D.; Lu, Z. P.; Liu, Z. Y.; Liang, L.; Chen, G. L. *J. Alloys Compd.,* **2009**, *467*, 187–190.

87. Lin, I.-C.; Lin, C.-J.; Tuan, W.-H. *Ceram. Int.,* **2013**, *39*, 8861–8864.

88. Abdelhafiz, A.; Wang, B.; Harutyunyan, A. R.; Li, J. *Adv. Energy Mater.* **2022**, *12*, 2200742.

89. Bykov, V. A.; Kulikova, T. V.; Sipatov, I. S.; Sterkhov, E. V.; Kovalenko, D. A.; Ryltsev, R. E. *Crystals,* **2023**, *13*, 1567.

90. Thermal Conductivity of Common Metals. https://www.engineersedge.com/heat_transfer/thermal-conductivity-metals-alloys.htm (accessed November 19, 2024).